Journal of the European Ceramic Society xxx (xxxx) xxx–xxx

Contents lists available at ScienceDirect

Journal of the European Ceramic Society

journal homepage: www.elsevier.com/locate/jeurceramsoc

Original Article

Cold sintering process of ZnO ceramics: Effect of the nanoparticle/microparticle ratio

Aída Serrano[a,*], Olga Caballero-Calero[b], Miguel Ángel García[a], Snežana Lazić[c], Noemi Carmona[d], Germán R. Castro[e,f], Marisol Martín-González[b], José F. Fernández[a]

[a] Departamento de Electrocerámica, Instituto de Cerámica y Vidrio (ICV), CSIC, E-28049, Madrid, Spain
[b] Instituto de Micro y Nanotecnología, IMN-CNM, CSIC (CEI UAM+CSIC), Isaac Newton 8, Tres Cantos, E-28760, Madrid, Spain
[c] Departamento de Física de Materiales, Instituto "Nicolás Cabrera" and Instituto de Física de Materia Condensada (IFIMAC), Universidad Autónoma de Madrid, E-28049 Madrid, Spain
[d] Departamento de Física de Materiales, Universidad Complutense de Madrid, E-28040 Madrid, Spain
[e] Spanish CRG BM25-SpLine at The ESRF, The European Synchrotron, F-38000 Grenoble, France
[f] Instituto de Ciencia de Materiales de Madrid (ICMM), CSIC, E-28049, Madrid, Spain

ARTICLE INFO

Keywords:
Cold sintering process
ZnO
Ceramic
Nanoparticles
Intrinsic defects
Photoluminescence

ABSTRACT

We show the efficiency in the preparation of > 95 % dense ZnO ceramics by cold sintering process through the incorporation of ZnO nanoparticles in the 1 − 10 wt% range at temperatures of 170 °C, pressures of 750 MPa and a pellet height/diameter ratio of 0.38. Morphological, structural and physical properties are dependent on the amount of ZnO nanoparticles incorporated into the system. After the densification by cold sintering process, ZnO ceramics show a reduction of the average valence indicating the deficiency of oxygen, similar to ceramics sintered by the conventional route. Besides, the generation of structural disorder and modifications into the ZnO lattice are identified in sintered ceramics, inducing intrinsic defects related to the loss of oxygen ions, the diffusion of zinc and zinc vacancies, which depend on the sintering process and the starting powders. These characteristics influence the final functional properties of the sintered ZnO ceramics, such as the visible photoluminescence signal.

1. Introduction

Semiconductors are materials with applications in the electronic industry, on which a large variety of the actual technological devices are based. Especially, zinc oxide (ZnO) is an n-type semiconductor with the bandgap around 3.37 eV at 300 K [1] and it is not only extensively used for electronic systems but also in other fields such as gas sensors, light-emitting diodes, solar cells, varistors and bactericidal applications [2]. As ceramic, ZnO is a remarkable material, although a large number of drawbacks can be involved in its structural and functional properties due to the exaggerated grain growth at high sintering temperatures (> 1000 °C) required to densify ZnO ceramics. A possibility to overcome these inconveniences is employing non-conventional sintering methodologies, which are designed to obtain both small grain sizes and high densification at the same time, as for example by the cold sintering process, CSP. CSP was developed by *C.A. Randall's group* in 2017 [3] in which at least one inorganic compound in particle form is mixed with a solvent that partially solubilizes it to promote the mass transport of powders when applying a uniaxial pressure at low temperatures (< 300 °C), making it a dense material [4–9]. Since then, the CSP has been employed for the sintering of a large number of binary, ternary and quaternary compounds, reducing temperatures and times in the sintering processes, thus leading to a breakthrough in the ceramic processing science. The CSP has even been used for the preparation of several composite structures from very dissimilar materials such as polymer/ceramics [6,10,11].

In the last few years, several works have been published about the densification of ZnO ceramics by CSP using an aqueous dissolution of acetic acid or zinc acetate as solvent [12–16]. Therefore, taking into account the feasibility of the method to prepare ZnO ceramics, the next natural step is focused on investigating both the structural and the functional properties obtained and how to optimize them. For instance, *Lowum et al.* presented a preliminary study on the mechanical properties on the ZnO ceramics sintered by CSP [14], *Gonzalez-Julian et al.* analyzed the defective grain boundaries [13] and *Jing et al.* studied the improvement of the electrical conductivity through post-annealing

* Corresponding author.
E-mail address: aida.serrano@icv.csic.es (A. Serrano).

https://doi.org/10.1016/j.jeurceramsoc.2020.05.059
Received 30 March 2020; Received in revised form 20 May 2020; Accepted 23 May 2020

treatments [15]. However, many aspects are still unclear and a wider research is still required to understand the effects in the structural and physical properties of the system depending on the starting products, their physical and chemical characteristics and the sintering conditions in CSP, which can induce new phenomenologies on the material characteristics.

In this work, we have sintered ZnO ceramics by the CSP using an aqueous dissolution of acetic acid and evaluated the influence of the fraction of starting microparticles (MPs) and nanoparticles (NPs) in the morphological and structural properties, as well as in the photoluminescence (PL) response. For such purposes, several parameters of the CSP such as the temperature and the ratio of the sintered pieces have been also assessed. Structural and physical properties of the CSP sintered ZnO ceramics are compared with those obtained from conventional (CN) sintering process and, in some cases, with the starting MPs and NPs powder properties. Tuneable structural and physical features such as the density, the size of the crystalline domain, the particle size, the Zn environment at short-range, the structural defects and the luminescence features of ZnO ceramics prepared by CSP are analyzed.

2. Materials & methods

ZnO MPs powders (average size 0.2 − 1 μm) from Asturiana de Cinc S.A. (Spain) and ZnO NPs powders (average size 20 − 100 nm) from Evonik Industries (Germany), manufactured via French process with a purity of > 99 %, were employed for the preparation of the ceramics. These MPs and NPs powders were dispersed by a dry method in order to avoid the agglomeration of the ZnO particles remaining their morphology unaltered [17]. CSP was performed using acetic acid as solvent with a 20 wt% 1 M aqueous solution. Prior to the cold sintering, powders were hand mixed in an agate mortar with the acid acetic solution to obtain a granulated powder. Granulates of powders were first pressed at 270 MPa for 5 min at room temperature (RT) in a cylindrical die with an inner diameter of 0.83 mm. Then, the pressed ZnO pellets were submitted to CSP in a Burkle D-7290 press, heating at a target temperature for 1 h and applying a pressure of 750 MPa. The annealing rate of 20 °C/min was used, and then cooled down in air. During the cold sintering method, some parameters were varied such as the height/diameter ratio of the pellets (from 0.17 to 0.44) and the target temperature (from 110 °C to 190 °C), in order to get the best ones. These processing parameters were studied to obtain the highest density values of the CSP ZnO pieces (see Supporting Information, SI). Both the pressure and the temperature values were not measured into the die, but are those registered in the pressing machine, that is, the nominal values. Once the CSP parameters were optimized, the effect of ZnO NPs in combination with MPs was evaluated. For that, the mixture of ZnO MPs and NPs powders was prepared at different percentages (0, 1, 5, 10, 30, 50 and 100 wt% of NPs) by a dry dispersion method for 10 min [17] and the final product in each case was submitted to CSP. The resulting samples were compared with ZnO pellets obtained by a CN method, which were pressed at 270 MPa and subsequently sintered at 1300 °C for 5 h in air using the same starting MPs and NPs powders. Table 1 shows both, the samples selected for this work using CSP by varying the fraction of NPs and the ceramics prepared by CN route.

The relative density of the sintered samples was determined by the Archimedes method and by the mass/dimension values, considering the theoretical ZnO density value of 5.605 g/cm^3 [18].

The grain morphology of the ZnO ceramics was studied by field emission scanning electron microscopy (FESEM) with an S-4700 Hitachi instrument at 20 kV on fresh fractured surfaces. ImageJ software was used to generate the particle size distribution based on the FESEM images and determine the average particle size. The crystalline phases of the initial products and sintered samples were characterized by X-ray diffraction (XRD, D8, Bruker) using a Lynx Eye detector and a Cu Kα radiation with a λ = 0.154 nm. By using the Debye-Scherrer equation the crystallite size of samples was determined from the fitting of Bragg peaks in the 2θ range of 25–80 deg, with the correction of the full width at half maximum (FWHM) for instrumental broadening. X-ray absorption spectroscopy (XAS) was performed on the sintered samples to evaluate the effect of the sintering method on oxidation state and ZnO short-range atomic structure: Zn coordination and the presence of defects. Samples were characterized at the Zn K-edge at the SpLine-CRG BM25 beamline at The European Synchrotron (ESRF), Grenoble (France). Measurements were collected at RT in fluorescence mode using a 13 element Si (Li) solid-state detector at 90° with respect to the incoming X-ray beam and with the sample surface placed at an angle of 45° to the incident source. The energy calibration was performed by a Zn foil standard. Starting ZnO powders (MPs and NPs) were measured as references in transmission detection mode employing ionization chambers. The XAS data were processed using Athena and Artemis software [19,20]. Raman characterization was performed at RT using a Witec ALPHA 300RA confocal Raman microscopy (CRM) with a linearly p-polarized Nd:YAG laser (532 nm). Raman measurements were performed by fixing the laser excitation power at 5 mW and using an objective with a numerical aperture (NA) of 0.95. Average Raman spectra were obtained from an in-plane mapping (10 × 5 μm^2) on the sample surface, where single Raman spectra were recorded every 300 nm. Raman measurements were analyzed by using Witec Control Plus Software. The time-integrated micro-photoluminescence (μ-PL) measurements were carried out in air at RT under continuous-wave optical excitation at 325 nm (Helium Cadmium laser from Kimmon). The laser beam was focused onto the sample surface by a ×50 microscope objective lens (Mitutoyo M Plan UV, NA = 0.41). The emitted light was collected by the same objective lens, dispersed by a single-grating monochromator (Horiba/Jobin Yvon 1000 M Series II, spectral resolution of ~350 μeV) and detected with a liquid nitrogen-cooled CCD camera (Symphony II from Horiba Scientific). To block the excitation laser from entering the monochromator, a 325 nm RazorEdge ultra-steep long-pass edge filter (Semrock LP03 − 325RE-25) was inserted in the optical collection path. The μ-PL signal was recorded for the excitation power density of ~8720 W/cm^2. Other excitation powers were evaluated with equivalent results.

Table 1
Description of samples sintered for this work, indicating the sintered methodology and the ZnO fraction of MPs:NPs starting powders. CN: conventional route and CSP: cold sintering process.

Sample	Starting powder ratio (wt%)	Sintering methodology
CSP n0	100 MPs	CSP
CSP n1	99 MPs:1 NPs	CSP
CSP n5	95 MPs:5 NPs	CSP
CSP n10	90 MPs:10 NPs	CSP
CSP n30	70 MPs:30 NPs	CSP
CSP n50	50 MPs:50 NPs	CSP
CSP n100	100 NPs	CSP
CN micro	100 MPs	CN
CN nano	100 NPs	CN

3. Results & discussion

3.1. Morphological and structural characterization

The CSP is a sintering route in which a large number of process parameters can be evaluated and optimized [4,8], which is an advantage both for densifying materials in a controlled way and tailoring the final properties of the sintered pieces. Here, an investigation on the incorporation of ZnO in its nano form into micro powders and its effect on the densification of the cold sintered ZnO samples is followed. A first study on both the optimal annealing temperature and the dimension ratio of the ceramic pieces is performed (see Figure S1 in SI). Significant

modifications depending on the CSP temperature are found: an increase of the relative density from 67 % for the sample prepared at 110 °C to relative density values around 95 % at processing temperatures of 170 °C–190 °C, densifying the ZnO ceramics at temperatures well below those used in the CN process in accordance with previously reported experiments [12,16]. On the other hand, fixing the CSP processing temperature to 170 °C, as the lowest temperature required to densify ZnO ceramics, relative density values close to 95 % are obtained for height/diameter ratio of pellets ≥ 0.38.

Therefore, the relative density of ZnO ceramics processed by CSP for different starting NPs:MPs fractions is evaluated at the optimized parameters of pressure, temperature and height/diameter ratio of 750 MPa, 170 °C and 0.38, respectively, at which the density values are as high as those obtained by CN methodology (see Figure S1 in SI). High relative density values are obtained for samples sintered with low NPs:MPs fractions (that is, CSP n0 - CSP n10). However, a change of trend is noted at a higher percentage of NPs with a decrease of the relative density to 94 % for CSP n30 and CSP n50, and achieving the lowest relative density, ~86 %, for CSP sample prepared from 100 wt% NPs (CSP n100). These results can be explained by the large quantity of agglomerates formed as the percentage of NPs increases, inducing a low compactability in the pellets of NPs/MPs-based compositions for proportions of NPs > 10 wt% [17]. Thus, it is concluded that ZnO ceramics are densified by optimizing several parameters in the CSP process, leading to even larger relative densities than those obtained by the CN route for proportions of ZnO NPs < 10 wt% in the starting powder mixture.

Long-range structural characterization of the CSP sintered ZnO ceramics has been carried out by means of XRD. Possible residual phases or structural modifications of the ZnO lattice in the samples prepared under the CSP conditions have been evaluated. Fig. 1a shows the XRD patterns related to samples prepared by CSP with different fractions of NPs, as well as those prepared by the CN method from pure MPs and NPs, for comparison. In all cases, only the wurtzite reflections are identified [21], and no other phases are detected within the detection limit. In addition, no significant variations are found in the diffraction pattern between the dense ceramics obtained by CSP varying the percentage of ZnO NPs and those obtained by the CN technique. However, modifications on the crystallite size are recognized (see Fig. 1b) depending on the sintered conditions and the starting powder. For the samples prepared by the CN method, a significant increase of the crystallite size is observed, from circa (ca.) 90 nm and ca. 32 nm for starting MPs and NPs, respectively, to 180 nm for sintered CN micro and 90 nm for sintered CN nano (see Fig. 1b). For the sintered CSP ceramics, the crystallite size reaches a maximum value of ca. 143 nm for a NPs percentage of 5−10 wt% (CSP n5 and CSP n10), which is higher than the crystallite size of the starting MPs, but does not reach the value obtained for the CN micro. As the NPs percentage increases in the starting powder, the ceramic crystallite size decreases up to ca. 47 nm for CSP n100, indicating a low crystallite size growth related to the starting ZnO NPs (32 nm).

For the samples sintered by CSP varying the process temperature and the pellet dimensions (used in the optimization study, shown in the SI), an increase of the crystallite size is found as the temperature and pellet ratio increase, as reported in the SI (Figure S3). Specifically, for the CSP sample sintered at 110 °C from 100 % MPs a crystallite size of ca. 97 nm is obtained displaying a slight growth of crystallite size even at the lowest CSP temperatures. The aqueous solution of acetic acid employed to sinter by CSP the ZnO facilitates the mass transport and the occurrence of the dissolution-precipitation processes, followed by a controlled evaporation of the aqueous solution that drives its supersaturation to allow the crystalline growth of ZnO grains [9,22]. During this process, the influence of the pellet die sealing needs to be mentioned. The appropriated sealing conditions allow the aqueous solution to be trapped favouring the dynamic, but also the leakage of a certain fraction by evaporation or extrusion process from the imperfectly sealed pellet die [23].

It should be noted that a similar tendency, qualitatively, is observed between the crystallite size and the relative density values of sintered samples (Fig. 1 and Figure S2), suggesting that the increasing effect of the crystallite size could correlate with the grain coarsening process during the densification process. While it is also possible a decrease in the grain size produced by the mass transport and dissolution/precipitation processes during the CSP [23]. Besides, larger crystallite sizes for ZnO ceramics processed by CN route than for CSP are identified, which can be attributed to an increased large activation energy for the grain growth during the solid-state sintering [12]. Therefore, both sintering processes and starting parameters influence the crystallite size of ZnO ceramics.

Fig. 2 shows the fracture cross-section micrographs obtained by CSP with different ZnO NPs:MPs fractions. A limited grain growth is identified with respect to the starting ZnO micropowder, which presents platelet-type morphology and some are large rod-like particles (see Figure S4 in SI). Specifically, for CSP n0 an average value of around 0.7 ± 0.4 μm is observed (Fig. 2a). Also, two main features are relevant in CSP n0: first, the grain morphology is similar to that of the starting powder but rod-like particles are deconstructed in platelet-type grains, and secondly, the local appearance of a non-crystalline intergrain phase. This secondary phase could be induced by the high chemical potential of particles due to their partial solubility through the acetic acid solution during the CSP, and represents a diffuse shell surrounding the grains in the FESEM micrographs. Its formation has already been reported in CSP sintered ZnO ceramics by Raman experiments [9,23], but here we show the first evidences of its presence by a microstructure characterization. For the CSP samples with less than 10 wt% of NPs, whose morphology is mostly platelet-type with some sintering necks between particles (see Figure S4 in SI), the average grain size is around 0.7 ± 0.3 μm (see Fig. 2b for sample CSP n10), identifying a more homogeneous grain size and most of grains surrounded by the secondary amorphous intergranular phase. However, increasing the ZnO

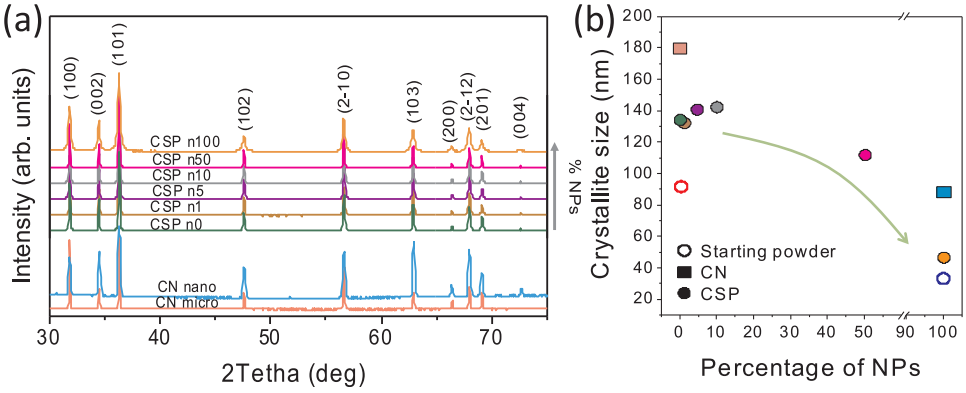

Fig. 1. (a) XRD patterns and (b) average crystallite size of the ZnO ceramics processed via CSP (filled circles) for different starting percentages of NPs and using the CN method (filled squares) from MPs and NPs (open circles). The average crystallite size of the starting ZnO powders (MPs and NPs) is also shown. Arrow on Fig. 1b shows the crystallite size evolution of CSP sintered ceramics increasing the percentage of NPs.

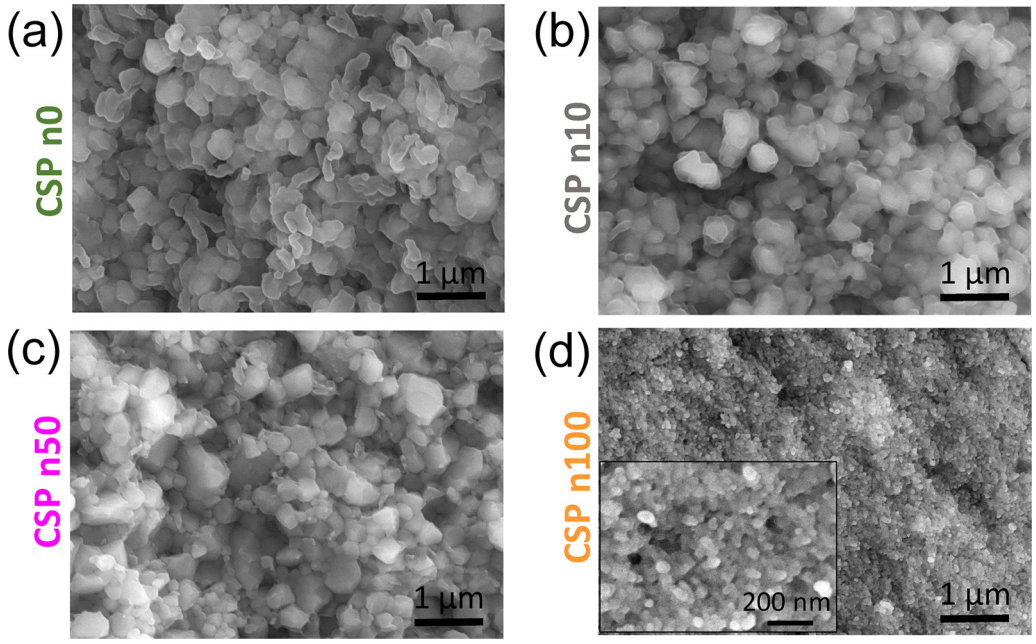

Fig. 2. FESEM micrographs of fresh fracture surface of CSP sintered ceramics: (a) CSP n0, (b) CSP n10, (c) CSP n50 and (d) CSP n100. The appearance of a non-crystalline intergrain secondary phase is identified for ZnO ceramics processed with low wt% of NPs (CSP n0-CSP n10).

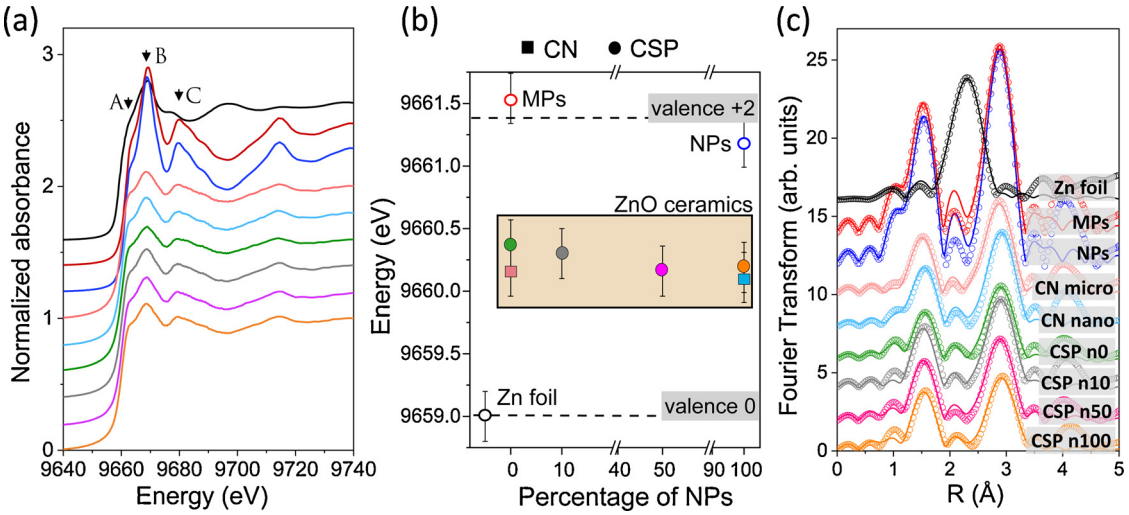

Fig. 3. (a) XANES spectra, (b) average valence from the position at the absorption edge in XANES region and (c) EXAFS spectra of the ZnO ceramics processed by CSP evaluating the % of NPs and compared with ceramics prepared by CN method. ZnO references from starting nano and micro powder form (NPs and MPs) and the Zn foil are also presented. An intermediate average valence for the sintered samples is identified between the values for Zn foil (valence 0) and the ZnO powder references (valence +2).

NPs proportion (> 10 wt%) causes the appearance of a dual microstructure in which submicronic grains with an average size of 0.6 ± 0.2 µm present nanograins with an average size of 120 ± 40 nm at the grain boundaries (Fig. 2c for sample CSP n50). This can be related to the fact that the fraction of ZnO NPs is relatively large to disolve in the aqueous solution of acetic acid. Besides, the secondary phase presence is apparently reduced when compared with the CSP sintered ceramics with lower ZnO NPs proportions (see CSP n10). The large quantity of nanograins presents a greater surface to be covered by the secondary phase, whose thickness surrounding the particles decreases considerably taking into account that its volume is constant. However, the microscope resolution does not allow to elucidate this aspect. This behaviour affects the ceramic densification, decreasing the relative density as is shown above. Specifically, for the CSP n100 (that is, with 100 % of ZnO NPs), the average grain size of 89 ± 46 nm is quite similar than that of the starting nanopowder (see Fig. 2d), indicating that sintering takes place without grain coarsening.

Comparing both sintering methodologies, a larger grain growth is achieved for CN sintered ceramics than in ZnO ceramics processed by CSP (see Figure S4 in SI). For CN micro irregular grains with an average value of 22 ± 9 µm are observed, without the presence of porosity. In addition, the presence of triple point junctions having 120° angles and straight grain boundaries indicates that the microstructural equilibrium is mostly attained in the sample. Conversely, the microstructure of sintered CN nano is more homogeneous with a lower grain size, 6 ± 2 µm, larger number of triple point junctions with 120° angles and residual porosity, which is closed indicating that the third stage of sintering is reached.

Although from a structural point of view the ZnO ceramics performed by CSP retain the same wurtzite structure than those sintered by

CN route according to the XRD results (Fig. 1), important modifications on the Zn and O stoichiometry could have happened during the different sintering processes. In order to investigate possible defects and in particular with the nature of the secondary phase identified by FESEM, and changes on the short-range ZnO structure induced during CSP, a series of XAS measurements have been carried out and compared with those performed on ZnO ceramics processed by the CN method.

X-ray absorption near-edge structure (XANES) measurements performed at the Zn K-edge of ZnO ceramics prepared by CSP and CN are shown in Fig. 3a, along with the starting MPs and NPs powders and a Zn foil used as references for comparison. At the whiteline of XANES spectra, the peaks labelled A, B, and C are identified, corresponding to electron transitions from the occupied Zn-1s to unoccupied Zn-4p states along the c, a and b axes of the ZnO unit cell, respectively [24,25]. From the intensity and energy position of those peaks, as reported in the literature, the occurrence of Zn and O vacancy positions can be deduced [24,26,27]. For example, similar absorption signal is observed comparing the ZnO ceramics sintered by CSP and CN method. However, for both sintering processes (CSP and CN), great modifications in the XANES region with respect to the reference materials (starting powders) can be distinguished. There is a clear decrease in the intensity of the peak B, as well as in the main resonances including the peak C (see Fig. 3a). This change in the intensity may be attributed to oxygen vacancies (V_O) of the ZnO lattice, according to *Haug et al.* from the calculated absorptions curves in ZnO bulk [24]. These results are confirmed through the absorption edge position of XANES region, for which a shift in the absorption edge towards lower energies is found, similar to other transition metals [28–30]. This indicates a reduction of the average oxidation state (a reduction of O atoms into the ZnO lattice) for the ZnO ceramics prepared by both the CSP and the CN method with respect to the starting powders, as illustrated in Fig. 3b, which suggests a larger number of V_O on average for the sintered samples. This reduction in the average oxidation state of the ZnO ceramics may be a consequence of the solution-precipitation process that occurs during the CSP and of the solid-state process at high temperatures in the CN samples, which induce both the intrinsic defect generation and the reduction of the specific surface [31]. During the sintering processes, the oxygen loss is promoted, generating superficial V_O and favouring the Zn diffusivity, which takes place through the formation of zinc interstitials (Zn_i) that are controlled by a zinc vacancy mechanism [32,33]. Here, these structural modifications can be confirmed, pointing out to the presence of V_O defects in the ZnO structure. It is also worth to mention that the results are equivalent for both ZnO sintering ceramic processes (CSP and CN route), in spite of the different temperatures employed during the sintering process. This suggests that the formation of defects, such as V_O, and the decrease of the average valence in the ZnO ceramics is more related to the sintering mechanisms. Despite the ceramics processed by CSP do not reach the same temperature as the ZnO sintered by CN at high temperatures, the V_O formation energy at low temperature under a specific pressure is low enough [34] to generate similar V_O concentrations than in CN route, which reduces the average oxidation state of ZnO ceramics. In addition, by CSP, it should be considered the dissolution of Zn^{2+} and O^{2-} ions on the surface ZnO particles in contact with the aqueous solution and the defect formation due to the diffusion of H^+ and OH- ions, among other effects. As a result, a high number of defects (including V_O) at the grain boundaries is generated reducing the formation energy of the atomic diffusion to sinter the CSP ZnO ceramics [13]. This may be corroborated with the reduction in the Zn-O coordination number at short-range in all sintered ceramics determined by EXAFS as shown below. With respect to the secondary phase identified in CSP sintered ceramics, no indication of other phases than that of ZnO is revealed by XANES technique which is considered a species-specific fingerprint [35].

The short-range ordering of cations around the Zn ions and the neighbour bondlengths are analyzed by extended X-ray absorption fine structure (EXAFS) technique in order to complement the XRD and XANES results, showing the influence of the sintering process in each case. Fig. 3c displays the modulus of the Fourier transform (FT) of the EXAFS signal at the Zn K-edge for ceramics prepared by CSP, CN method, the starting powders and Zn metal foil. The FT is performed in the $k^2\chi(k)$ weighted EXAFS signal between 2.5 and 11.0 $Å^{-1}$. Experimental EXAFS results are fitted in R-space in the range 1.5–3.5 Å (first and second shell) using the FEFFIT code [19]. The fitting was performed by fixing the shift at the edge energy E_0 for each type of neighbour ions, which were previously calculated from the starting ZnO MPs (used as reference). Therefore, the coordination number N, the interatomic distance R and the Debye-Waller (DW) factors σ^2 for the first and second shells are used as free parameters. For the fitting, a first shell produced by the interaction of a Zn absorbing atom with four oxygen atoms and a second one constituted by two shells of six Zn atoms each are considered. The numerical EXAFS results obtained from the fitting for sintered ZnO ceramics prepared by CSP and CN method, as well as for MPs and NPs references and Zn foil, are displayed in Table S2 in SI.

As Fig. 3c shows, the EXAFS signal of the different samples presents two shells in which variations in the position and amplitude of both are identified depending on the preparation process. For the MPs and NPs ZnO powders, similar DW factors and neighbour distances are obtained. On the contrary, an increase of the coordination number for the NPs is obtained in both Zn-O and Zn-Zn shells (see Table S2 in SI). As the ZnO powders are densified both by the CN route and CSP, the largest variations on the O and Zn coordination at short-range are found, reaching less than half the value in the coordination number compared to the MPs and NPs. These results may be correlated to the intensity reduction of resonances in the XANES signal and the energy shift at the absorption edge to lower energies showing a reduction of the average of oxidation state on Zn ions in ZnO ceramics prepared by both sintering processes (see Fig. 3). Besides, for the samples prepared by CSP varying the NPs:MPs fraction a trend can be identified: the greater is the NPs proportion, the larger is the coordination number at the Zn-O and Zn-Zn first shells.

Additionally, a slight increase in the distance of first neighbours at the first shell is recognized as the NPs are incorporated both in the CN and CSP samples (see Table S2 in SI). These results may induce the presence of the structural disorder noted at short range to accommodate the second shell of the ZnO structure with the consequent increase of the DW factor, being larger for the sample CSP n100 where a larger number of intrinsic structural defects as Zn_i may be the responsible ones.

A Raman characterization on ZnO ceramics sintered by both routes (CSP and CN) and the starting ZnO powders (MPs and NPs) is also performed to explore the final structural properties of ZnO ceramics, as shown in Fig. 4. The active vibration modes in the Raman spectrum of ZnO structure have been previously assigned in the literature [36–39], and a detailed description is provided in the SI. The identification of the main Raman vibrations modes is carried out on Fig. 4, detecting several changes in the intensity, the position and the FWHM of some Raman modes. For instance, starting MPs and NPs powders show significant intensity differences in some vibrational Raman bands: $A_1(TO)$ mode is more intense for the ZnO MPs while the $2LA$ mode is larger in the NPs, which indicates high polarizability changes of the ZnO crystal in each case.

For the ZnO ceramics sintered by CN route, more intense Raman signals in the $A_1(TO)$, $E_1(TO)$, E_2^h, $A_1(LO)$ and $E_1(LO)$ vibrational bands with respect to the reference powders are identified, being more pronounced for the TO and E_2^h modes in the case of the CN micro and the LO ones in the CN nano. The intensity increase in E_2^h band for CN micro may be related to domination of oxygen defects after the sintering [38] which can be associated with V_O defects, as were found them to be greater for the CN micro by the XAS results. In the case of the higher activation of LO modes in the ceramic CN nano, it can indicate the presence of a large concentration of intrinsic lattice defects in the

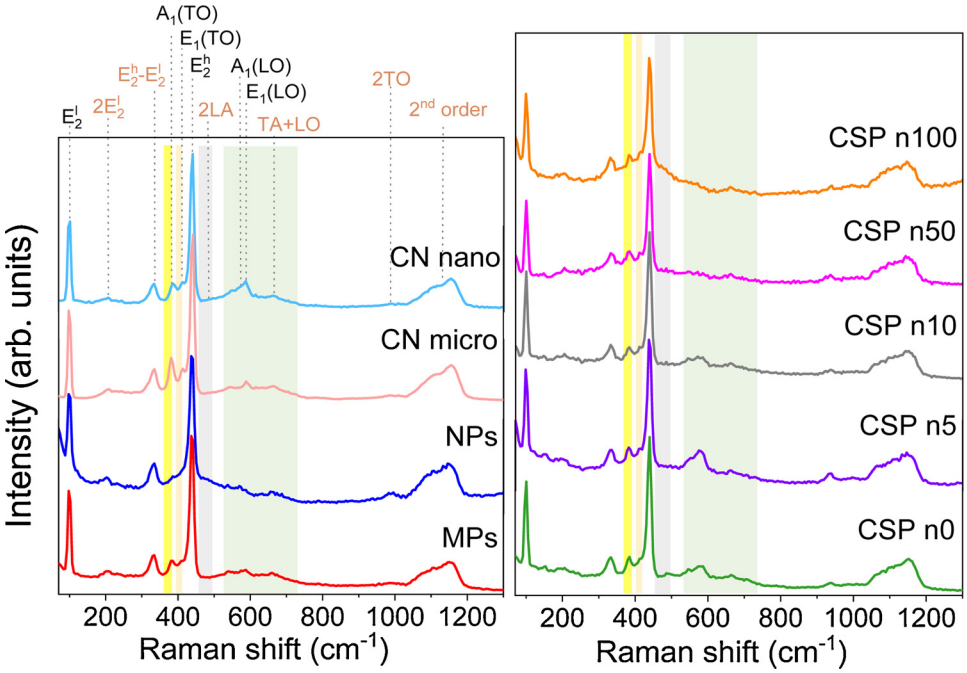

Fig. 4. Raman measurements of the ZnO ceramics prepared by CSP modifying the wt% of NPs and MPs in the starting powder: CSP n0, CSP n5, CSP 10, CSP n50 and CSP n100. The Raman spectra for ZnO MPs and NPs references in powder form and the ZnO ceramics processed by the CN route from MPs and NPs powders at 1300 °C for 5 h (CN micro and CN nano) are also presented. Spectra are displayed from 70 to 1300 cm^{-1}. Assignment of Raman modes of ZnO is shown in the figure.

ZnO structure [37] that may be correlated with the large DW factors (within the error), meaning a large disorder in the lattice for the nanosystems. Besides, an intensity decrease of 2*LA* for the CN nano with respect to the starting powders is observed.

In the sample prepared by CSP entirely from MPs (CSP n0), an intensity increase of $A_1(LO)$, $E_1(LO)$, 2*LA* and 2*TO* vibrational modes with respect to the starting MPs can be observed. This increase is larger with the incorporation of 5 wt% of ZnO NPs in the system (sample CSP n5). Moreover, in this case, the $E_1(TO)$ intensity also increases with respect to the starting powder. Further increase of the NPs content to 10 wt% (CSP n10) presents a different trend, with a decrease of $A_1(LO)$, $E_1(LO)$ and 2*TO* vibrational bands, which continue diminishing up to the sample with a 50 wt% of NPs (CSP n50), where it is possible to appreciate an increase of the 2*LA* mode. These results are accentuated for the sample prepared from 100 wt% NPs (CSP n100), where a similar Raman signal to the starting ZnO NPs is found.

Specifically, comparing the samples prepared by CN and CSP from 100 wt% NPs, large differences are noted: a more intense 2*LA* mode is identified in the sample CSP n100 and more intense $A_1(LO)$ and $E_1(LO)$ bands are identified in the CN nano. Although from XAS experiments a similar oxygen deficiency and short-range ordering were deduced, a large structural disorder (DW factor) was obtained in the sample prepared by CSP (CSP n100). That may relate to the great intensity of 2*LA* band in Raman spectrum characteristics of the nanopowder (see Fig. 4) and may indicate a sintering with structural features similar to the starting powders. This observation is confirmed from the obtained densification values and XRD data. For samples prepared from 100 wt% MPs, an intensity increase of $A_1(TO)$ and $E_1(TO)$ modes for the CN micro and of $A_1(LO)$, $E_1(LO)$, 2*LA* and 2*TO* modes for the CSP n0 are observed, which may be attributed to a larger concentration of intrinsic defects in the ZnO structure for the sample prepared by CSP where the secondary phase presence could be influencing. These results agree with EXAFS fittings (Fig. 3c and Table S2 in SI) with a slightly lower coordination number (in both shells), a larger distance of first neighbours and a larger DW factor (structural disorder) for the CSP n0 when compared to CN micro.

Therefore, both methodologies of sintering (CN method and CSP) induce the generation of structural disorder and modifications into the ZnO lattice, resulting in defects related to the loss of oxygen ions, the diffusion of Zn_i and zinc vacancies (V_{Zn}), which depend on the sintering process and the starting powders. These differences between the different methods and starting powders should influence their functional properties, such as the PL signal, discussed below.

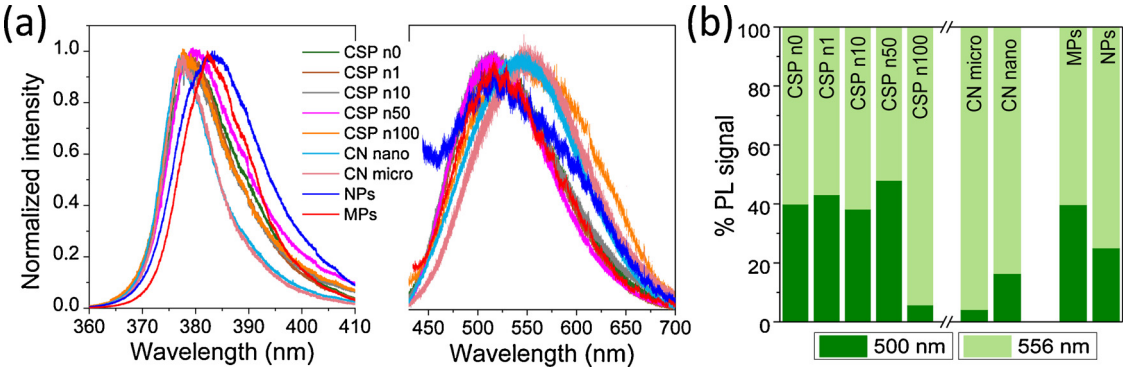

Fig. 5. (a) PL response of the ZnO ceramics processed by the CN route from starting ZnO MPs and NPs (CN micro and CN nano), CSP modifying the fraction of NPs and MPs in the starting powder: CSP n0, CSP n1, CSP 10, CSP n50 and CSP n100, and the starting MPs and NPs. (b) Semi-qualitative analysis of the PL signal percentage related to the 500 nm and 556 nm emission band for each sample.

3.2. Photoluminescence response

Fig. 5a shows the μ-PL spectra from ZnO ceramics prepared both by CSP and CN method, along with the starting ZnO MPs and NPs. The first observation is that all of them display similar features: the first PL emission band around 378 nm, corresponding to a 3.28 eV energy and associated with the ZnO bandgap emission [36,40,41] and a second broad PL emission band located in the spectral range of 450–650 nm. The latter can be related to the presence of intrinsic defects in the ZnO structure and assigned to deep level emissions (DLE) [41–43]. In this case, a deconvolution of this second broad emission using two green emission bands is performed: one centred at 2.23 eV (556 nm) and another at 2.48 eV (500 nm). The area fraction of each contribution for the different samples is presented in Fig. 5b.

In the literature, the most generalized assignment of the 500 nm band is related to electronic transitions from the conduction band to V_O defects, while the emission located at 556 nm is sometimes attributed to transitions from Zn_i to V_O defects [40], or also to different luminescence centres, such as V_{Zn}, V_O, interstitial oxygen (O_i), Zn_i, anti-site oxygen (O_{Zn}) and their complexes [40,41,43–45]. However, taking account the XAS and Raman results, a direct assignation between the defects and the PL curves is not possible. In addition, despite the number of investigations related to the green luminescence, there are still many contradictions and many researchers conclude that the green emission in ZnO can be explained by the combination of several deep levels [40,46,47].

In our case, several factors can affect the luminescence response and different possibilities can explain the variations in the green range of the PL DLE. The properties of ZnO ceramics are strongly dependent on the starting material and the sintering process that induce changes in the grain sizes, surface, morphologies and defects, presenting important variations in their optical properties and specifically in their luminescence [48,49]. For example, changes in the PL properties may be induced by variations in the average ZnO particles sizes and morphology [50–52], but also changes corresponding to the optical band gap can be identified [52].

Depending on the sample, different contributions due to each of the green emission bands are found, as represented in Fig. 5. While samples processed by CN route show a greater proportion related to the green emission close to 556 nm, the ZnO ceramics prepared by the non-conventional method (CSP) present a larger contribution for the band of 500 nm, except from the sample fabricated from 100 wt% NPs of starting powder. Specifically, for the sample CSP n100 the surface/volume ratio is clearly larger than for the rest of ceramics sintered where a large number of Zn_i could be located at the interface grains which may explain the larger 556 nm emission with respect to the rest of CSP samples, corroborating the EXAFS results. For the case of CN ceramics, the greater emission to 556 nm may be related to the high temperature of the sintering process at which a larger number of luminescence centres might be generated with a selective green emission. With respect to the ZnO starting powders (MPs and NPs), an intermediate ratio between PL emission related to the ZnO ceramics prepared by CSP and CN route is obtained, with a larger signal of 556 nm band in ZnO NPs that may be attributed to the high surface/volume ratio of nanostructures with more Zn_i defects. In addition, the broadening of the emission curve varies depending on the ceramic, which could be assigned to the combination of different deep levels [46].

The ZnO ceramics prepared by both methodologies, according to the EXAFS results, presented above, contain both V_O and V_{Zn}. However, during the processing of the ceramics, other intrinsic defects, which have not been identified, may exist, as for example interstitials or anti-sites, which may be involved in the PL signal to generate the final green emission. In addition, the presence of the secondary amorphous phase identified in CSP sintered ceramics may induce some phenomenology involved in the final PL response. Therefore, even though it is not possible to assign a certain type of intrinsic defect to each green emission band, it is clear that optical results depend on the starting powder and most significantly on the processing method. This dependence opens the door to a possible control on both the position of the optical bandgap and the PL DLE of the ZnO ceramics.

4. Conclusions

The fabrication of dense ZnO ceramics has been feasible by the cold sintering process through the incorporation of a determined fraction of ZnO nanoparticles in a microparticle matrix. Relative density values > 95 % are obtained by the incorporation of ZnO nanostructures in the 1 − 10 wt% range. Morphological, structural and optical features of final ceramics depend on ZnO nanoparticle/microparticle ratio in the system, with the ZnO particles retaining their identity. By cold sintering route, the presence of a secondary amorphous intergrain phase has been identified limiting the crystallite size and the particle size. Results at the short-range ordering of cations around the Zn ions are quantified identifying an increase in both the first O and Zn neighbour distance, as well as an increasing structural disorder, as the proportion of ZnO nanoparticles increases. Besides, a reduction of the oxidation state and the generation of specific intrinsic defects are identified in all the sintered ceramics, independently of the preparation method, but with characteristics dependent on the sintering process and the starting powders. The final optical response of ZnO ceramics is also influenced by the processing route and the starting powder, presenting a green emission that can be tailored.

Author contributions

All authors have approved the final version of the manuscript.

Declaration of Competing Interest

The authors declare no competing financial interest.

Acknowledgements

This work has been supported by the Ministerio Español de Ciencia, Innovación y Universidades (MCIU) through the projects MAT2017-86540-C4-1-R, MAT2017-86540-C4-3-R and RTI2018-095303-A-C52. The European Synchrotron (ESRF), MCIU and Consejo Superior de Investigaciones Cientificas (CSIC) are acknowledged for the provision of synchrotron radiation facilities. We also thank the BM25-SpLine staff for the technical support beyond their duties. A.S. acknowledges financial support from the Comunidad de Madrid for an “Atracción de Talento Investigador” contract (No. 2017-t2/IND5395).

Appendix A. Supplementary data

Supplementary data associated with this article can be found, in the online version, at https://doi.org/10.1016/j.jeurceramsoc.2020.05.059.

References

[1] A. Janotti, C.G. Van De Walle, Fundamentals of zinc oxide as a semiconductor, Rep. Prog. Phys. 72 (2009) 12, https://doi.org/10.1088/0034-4885/72/12/126501.
[2] B. Dargatz, J. Gonzalez-Julian, O. Guillon, Improved compaction of ZnO nanopowder triggered by the presence of acetate and its effect on sintering, Sci. Technol. Adv. Mater. 16 (2015) 025008, , https://doi.org/10.1088/1468-6996/16/2/025008.
[3] H.G. Clive, A. Randall, Jing Guo, Amanda Baker, Michael Lanagan, Cold Sintering Ceramic and Composites US2017088471A1, (2017).
[4] J.P. Maria, X. Kang, R.D. Floyd, E.C. Dickey, H. Guo, J. Guo, et al., Cold sintering: current status and prospects, J. Mater. Res. 32 (2017) 3205–3218, https://doi.org/10.1557/jmr.2017.262.
[5] D. Wang, H. Guo, C.S. Morandi, C.A. Randall, S. Trolier-McKinstry, Cold sintering and electrical characterization of lead zirconate titanate piezoelectric ceramics, APL

Mater. 6 (2018) 016101, , https://doi.org/10.1063/1.5004420.
[6] J. Guo, S.S. Berbano, H. Guo, A.L. Baker, M.T. Lanagan, C.A. Randall, Cold sintering process of composites: bridging the processing temperature gap of ceramic and polymer materials, Adv. Funct. Mater. 26 (2016) 7115–7121, https://doi.org/10.1002/adfm.201602489.
[7] M. Biesuz, G. Taveri, A.I. Duff, E. Olevsky, D. Zhu, C. Hu, et al., A theoretical analysis of cold sintering, Adv. Appl. Ceram. 119 (2020) 75–89, https://doi.org/10.1080/17436753.2019.1692173.
[8] S. Grasso, M. Biesuz, L. Zoli, G. Taveri, A.I. Duff, D. Ke, et al., A review of cold sintering processes, Adv. Appl. Ceram. 119 (2020) 115–143, https://doi.org/10.1080/17436753.2019.1706825.
[9] J. Andrews, D. Button, I.M. Reaney, Advances in cold sintering, Johnson Matthey Technol. Rev. 64 (2020) 2, https://doi.org/10.1595/205651320x15814150061554.
[10] J. Guo, B. Legum, B. Anasori, K. Wang, P. Lelyukh, Y. Gogotsi, et al., Cold sintered ceramic nanocomposites of 2D MXene and zinc oxide, Adv. Mater. 30 (2018) 1–6, https://doi.org/10.1002/adma.201801846.
[11] A. Baker, H. Guo, J. Guo, C. Randall, D.J. Green, Utilizing the cold sintering process for flexible–Printable electroceramic device fabrication, J. Am. Ceram. Soc. 99 (2016) 3202–3204, https://doi.org/10.1111/jace.14467.
[12] S. Funahashi, J. Guo, H. Guo, K. Wang, A.L. Baker, K. Shiratsuyu, et al., Demonstration of the cold sintering process study for the densification and grain growth of ZnO ceramics, J. Am. Ceram. Soc. 100 (2017) 546–553, https://doi.org/10.1111/jace.14617.
[13] J. Gonzalez-Julian, K. Neuhaus, M. Bernemann, J. Pereira da Silva, A. Laptev, M. Bram, et al., Unveiling the mechanisms of cold sintering of ZnO at 250 °C by varying applied stress and characterizing grain boundaries by Kelvin Probe Force Microscopy, Acta Mater. 144 (2018) 116–128, https://doi.org/10.1016/j.actamat.2017.10.055.
[14] S. Lowum, R. Floyd, R. Bermejo, J.P. Maria, Mechanical strength of cold-sintered zinc oxide under biaxial bending, J. Mater. Sci. 54 (2019) 4518–4522, https://doi.org/10.1007/s10853-018-3173-8.
[15] Y. Jing, N. Luo, S. Wu, K. Han, X. Wang, L. Miao, et al., Remarkably improved electrical conductivity of ZnO ceramics by cold sintering and post-heat-treatment, Ceram. Int. 44 (2018) 20570–20574, https://doi.org/10.1016/j.ceramint.2018.07.192.
[16] X. Jiang, G. Zhu, H. Xu, L. Dong, J. Song, X. Zhang, et al., Preparation of high density ZnO ceramics by the Cold Sintering process, Ceram. Int. 45 (2019) 17382–17386, https://doi.org/10.1016/j.ceramint.2019.05.298.
[17] I. Lorite, J.J. Romero, J.F. Fernandez, Study of the nanoparticle/microparticle powder systems by dry dispersion, Ceram. Int. 39 (2013) 1631–1637, https://doi.org/10.1016/j.ceramint.2012.08.005.
[18] C. Jagadish, S. Pearton, Zinc Oxide Bulk, Thin Films and Nanostructures Processing, Properties and Applications, Elsevier: Amsterdam, The Netherlands, 2006.
[19] M. Newville, B. Ravel, D. Haskel, J.J. Rehra, E.A. Stern, Y. Yacoby, Analysis of multiple-scattering XAFS data using theoretical standards, Physica B 208-209 (1995) 154–156, https://doi.org/10.1016/0921-4526(94)00655-F.
[20] B. Ravel, M. Newville, ATHENA, ARTEMIS, HEPHAESTUS : data analysis for X-ray absorption spectroscopy using IFEFFIT, J. Synchrotron Radiat. 12 (2005) 537–541, https://doi.org/10.1107/S0909049505012719.
[21] K. Kihara, G. Donnay, Anharmonic Thermal Vibrations in ZnO, Can, Mineral. 23 (1985) 647–654.
[22] H. Guo, A. Baker, J. Guo, C.A. Randall, Cold sintering process: a novel technique for low-temperature ceramic processing of ferroelectrics, J. Am. Ceram. Soc. 99 (2016) 3489–3507, https://doi.org/10.1111/jace.14554.
[23] X. Kang, R. Floyd, S. Lowum, M. Cabral, E. Dickey, J.P. Maria, Mechanism studies of hydrothermal cold sintering of zinc oxide at near room temperature, J. Am. Ceram. Soc. 102 (2019) 4459–4469, https://doi.org/10.1111/jace.16340.
[24] J. Haug, A. Chassé, M. Dubiel, C. Eisenschmidt, M. Khalid, A. Chasse, Characterization of lattice defects by x-ray absorption spectroscopy at the Zn K-edge in ferromagnetic, pure ZnO films Characterization of lattice defects by x-ray absorption spectroscopy at the Zn K-edge in ferromagnetic, pure ZnO films 110 (2011) 063507, , https://doi.org/10.1063/1.3631774.
[25] D. Gallach, A. Muñoz-Noval, V. Torres-Costa, M. Manso-Silván, Luminescence and fine structure correlation in ZnO permeated porous silicon nanocomposites, Phys. Chem. Chem. Phys. 17 (2015) 20597–20604, https://doi.org/10.1039/c5cp02587g.
[26] R. Revel, D. Bazin, A.M. Flank, Influence of cations vacancies on the K and LIII Zn edges of spinel-related compounds, J. Synchrotron Radiat. 6 (1999) 717–718, https://doi.org/10.1107/S0909049599000916.
[27] A. Kuzmin, S. Larcheri, F. Rocca, Zn K-edge XANES in nanocrystalline ZnO, J. Phys. Conf. Ser. 93 (2007) 2–8, https://doi.org/10.1088/1742-6596/93/1/012045.
[28] M. Abuin, A. Serrano, J. Chaboy, M.A. Garcia, N. Carmona, XAS study of Mn, Fe and Cu as indicators of historical glass decay, J. Anal. At. Spectrom. 28 (2013) 1118–1124, https://doi.org/10.1039/C3JA30374H.
[29] J. Rubio-Zuazo, A. Chainani, M. Taguchi, D. Malterre, A. Serrano, G.R. Castro, Electronic structure of FeO, γ-Fe2O3, and Fe3O4 epitaxial films using high-energy spectroscopies, Phys. Rev. B 97 (2018) 235148, , https://doi.org/10.1103/PhysRevB.97.235148.
[30] S. Ruiz-Gómez, A. Serrano, R. Guerrero, M. Muñoz, I. Lucas, M. Foerster, et al., Highly Bi-doped Cu thin films with large spin-mixing conductance, APL Mater. 6 (2018) 101107, , https://doi.org/10.1063/1.5049944.
[31] F. Rubio-Marcos, A. Quesada, M.A. García, M.A. Bañares, J.L.G. Fierro, M.S. Martín-Gonzalez, et al., Some clues about the interphase reaction between ZnO and MnO2 oxides, J. Solid State Chem. 182 (2009) 1211–1216, https://doi.org/10.1016/j.jssc.2009.02.009.
[32] M.G. Cattania, P. d'Antona, F. Morazzoni, R. Scotti, Characterization of defects on ZnO and RuZnO: a structural, TPD, and spectroscopic study, Vacuum. 41 (7-9) (1990) 1633–1635, https://doi.org/10.1016/0042-207X(90)94038-R.
[33] G.W. Tomlins, J.L. Routbort, T.O. Mason, Zinc self-diffusion, electrical properties, and defect structure of undoped, single crystal zinc oxide, J. Appl. Phys. 87 (2000) 117–123, https://doi.org/10.1063/1.371832.
[34] I. Tanaka, F. Oba, K. Tatsumi, M. Kunisu, M. Nakano, H. Adachi, Theoretical formation energy of oxygen-vacancies in oxides, Mater. Trans. 43 (2002) 1426–1429, https://doi.org/10.2320/matertrans.43.1426.
[35] A. Ricci, L. Massaccesi, D. Pezzolla, G. Corti, A. Agnelli, G. Gigliotti, Multi-approach characterization of organic sediment produced by an anaerobic digestion plant fed with pig slurry and stored for a long term in a lagoon, J. Hazard. Mater. 330 (2017) 29–35, https://doi.org/10.1016/j.jhazmat.2017.02.003.
[36] R. Zhang, P.G. Yin, N. Wang, L. Guo, Photoluminescence and Raman scattering of ZnO nanorods, Solid State Sci. 11 (2009) 865–869, https://doi.org/10.1016/j.solidstatesciences.2008.10.016.
[37] R. Cuscó, E. Alarcón-Lladó, J. Ibáñez, L. Artús, Temperature dependence of Raman scattering in ZnO, Phys. Rev. B 75 (2007) 165202, , https://doi.org/10.1103/PhysRevB.75.165202.
[38] M. Šćepanović, M. Grujić-Brojčin, K. Vojisavljević, S. Bernikc, T. Srećković, Raman study of structural disorder in ZnO nanopowders, J. Raman Spectrosc. 41 (2010) 914–921, https://doi.org/10.1002/jrs.2546.
[39] E. de Lucas-Gil, A. Del Campo, L. Pascual, M. Monte-Serrano, J. Menéndez, J.F. Fernández, et al., The fight against multidrug-resistant organisms: the role of ZnO crystalline defects, Mater. Sci. Eng. C. 99 (2019) 575–581, https://doi.org/10.1016/j.msec.2019.02.004.
[40] P.A. Rodnyi, I.V. Khodyuk, Optical and luminescence properties of zinc oxide (Review), Opt. Spectrosc. English Transl. Opt. i Spektrosk 111 (2011) 776–785, https://doi.org/10.1134/S0030400X11120216.
[41] M.A. Garcia, J.M. Merino, E.F. Pinel, A. Quesada, J. De La Venta, M.L.R. González, et al., Magnetic properties of ZnO nanoparticles, Nano Lett. 7 (2007) 1489–1494, https://doi.org/10.1021/nl070198m.
[42] T. Dixit, I.A. Palani, V. Singh, Insights into non-noble metal based nanophotonics: exploration of Cr-coated ZnO nanorods for optoelectronic applications, RSC Adv. 8 (2018) 6820–6833, https://doi.org/10.1039/c7ra13174g.
[43] T.M. Børseth, B.G. Svensson, A.Y. Kuznetsov, P. Klason, Q.X. Zhao, M. Willander, Identification of oxygen and zinc vacancy optical signals in ZnO, Appl. Phys. Lett. 89 (2006) 1–4, https://doi.org/10.1063/1.2424641.
[44] R. Raji, K.G. Gopchandran, ZnO nanostructures with tunable visible luminescence: effects of kinetics of chemical reduction and annealing, J. Sci. Adv. Mater. Devices. 2 (2017) 51–58, https://doi.org/10.1016/j.jsamd.2017.02.002.
[45] M. Willander, O. Nur, J.R. Sadaf, M.I. Qadir, S. Zaman, A. Zainelabdin, et al., Luminescence from zinc oxide nanostructures and polymers and their hybrid devices, Materials (Basel). 3 (2010) 2643–2667, https://doi.org/10.3390/ma3042643.
[46] V. Herrera, T. Díaz-Becerril, E. Reyes-Cervantes, G. García-Salgado, R. Galeazzi, C. Morales, et al., Highly visible photoluminescence from Ta-doped structures of ZnO films grown by HFCVD, Crystals. 8 (2018) 395, https://doi.org/10.3390/cryst8100395.
[47] Y.H. Leung, X.Y. Chen, A.M.C. Ng, M.Y. Guo, F.Z. Liu, A.B. Djurišić, et al., Green emission in ZnO nanostructures - Examination of the roles of oxygen and zinc vacancies, Appl. Surf. Sci. 271 (2013) 202–209, https://doi.org/10.1016/j.apsusc.2013.01.160.
[48] Naeem-ur-Rehman, M. Mehmood, S.M. Ali, S.M. Ramay, M.A. Shar, M.S. AlGarawi, Annealing induced defects in ZnO nanostructures, Appl. Phys. A Mater. Sci. Process. 125 (2019) 1–8, https://doi.org/10.1007/s00339-019-2802-7.
[49] V. Khomchenko, M. Sopinskyy, M. Mazin, V. Dan'ko, O. Lytvyn, Y. Piryatinskii, The violet luminescence band in ZnO and ZnO-Ag thin films, J. Lumin. 213 (2019) 519–524, https://doi.org/10.1016/j.jlumin.2019.04.045.
[50] K.A. Eswar, J. Rouhi, H.F. Husairi, M. Rusop, S. Abdullah, Annealing heat treatment of ZnO nanoparticles grown on porous si substrate using spin-coating method, Adv. Mater. Sci. Eng. Int. J. 2014 (2014) 796759, , https://doi.org/10.1155/2014/796759.
[51] G.H. Mhlongo, D.E. Motaung, S.S. Nkosi, H.C. Swart, G.F. Malgas, K.T. Hillie, et al., Temperature-dependence on the structural, optical, and paramagnetic properties of ZnO nanostructures, Appl. Surf. Sci. 293 (2014) 62–70, https://doi.org/10.1016/j.apsusc.2013.12.076.
[52] N.M.A. Hadia, S. García-Granda, J.R. García, Effect of the temperature on structural and optical properties of zinc oxide nanoparticles, J. Nanosci. Nanotechnol. 14 (2014) 5443–5448, https://doi.org/10.1166/jnn.2014.8861.